Ti-bearing lightweight steel with large high temperature ductility via thermally stable multi-phase microstructure

Joonoh Moon [a,*], Hyo-Haeng Jo [a], Seong-Jun Park [a], Sung-Dae Kim [a], Tae-Ho Lee [a], Chang-Hoon Lee [a], Myoung-Gyu Lee [b], Hyun-Uk Hong [c], Dong-Woo Suh [d], Dierk Raabe [e]

[a] Steel Department, Advanced Metals Division, Korea Institute of Materials Science, 797 Changwondae-ro, Seongsan-gu, Changwon, Gyeongnam, 51508, Republic of Korea
[b] Department of Materials Science and Engineering, Seoul National University, 1 Gwanak-ro, Gwanak-gu, Seoul, 08826, Republic of Korea
[c] Department of Materials Science and Engineering, Changwon National University, 20 Changwondaehak-ro, Uichang-gu, Changwon, Gyeongnam, 51140, Republic of Korea
[d] Graduate Institute of Ferrous Technology, Pohang University of Science and Technology, 77 Cheongam-ro, Nam-gu, Gyeongbuk, 37666, Republic of Korea
[e] Max-Planck-Institut für Eisenforschung, Max-Planck-Straße 1, Düsseldorf, 40237, Germany

ARTICLE INFO

ABSTRACT

The global demand for lightweight design is increasing to provide sustainable solutions to counteract climate change. We developed a novel Ti-bearing lightweight steel (8% lower mass density than general steels), which exhibits an excellent combination of strength (491 MPa ultimate tensile strength) and tensile ductility (31%) at elevated temperature (600 °C). The developed steel is suitable for parts subjected to high temperature at reduced dynamical load. The composition of the developed steel (Fe–20Mn–6Ti–3Al–0.06C–NbNi (wt%)) lends the alloy a multiphase structure with austenite matrix, partially ordered ferrite, Fe_2Ti Laves phase, and fine MC carbides. At elevated temperature (600 °C), the ductility of the new material is at least 2.5 times higher than that of conventional lightweight steels based on the Fe–Mn–Al system, which become brittle at elevated temperatures due to the inter/intragranular precipitation of κ-carbides. This is achieved by the high thermal stability of its microstructure and the avoidance of brittle κ-carbides in this temperature range.

1. Introduction

With a production of 1.8 billion tons per year and use in multiple key products ranging from magnets to large infrastructures and vehicles, steel is the backbone material of modern society.

Despite its success, limitations emerge because of the high mass density (~7.9 g/cm³) of steels, which counteracts sustainability [1]. This motivates the demand for lightweight steels [2–13]. Fe–Mn–Al–C-based alloys were thus developed to serve this need at low costs. They have several excellent characteristics, including low mass density, high strength, and good ductility [2]. Al is very effective in this respect as it reduces the mass density of steel by about 0.1 g/cm³ per 1 wt% Al. However, the formation of brittle intermetallic precipitates limits this alloying strategy [2]. This can be omitted by adding alloying elements such as Mn and C, so that the matrix phase of Fe–Mn–Al–C steels can be composition-tuned into ferrite, austenite, or duplex microstructures, containing several types of precipitates [2].

While Fe–Al based ferritic steels with less than 8 wt% Mn have relatively low strength (<700 MPa ultimate tensile strength) and ductility (10–40%), Fe–Mn–Al–C based duplex and austenitic steels exhibit high strength (up to 1300 MPa ultimate tensile strength) and large ductility (up to 100%) when more C and Mn are added [2–4]. κ-carbide, which has an ordered face-centered cubic (FCC) structure with nominal stoichiometry of $(Fe,Mn)_3AlC$, is a very important precipitate for achieving ultra-high strength in Fe–Mn–Al–C based steels [2, 7]. Frommeyer et al. [8] developed TRIPLEX lightweight steel based on the system Fe–(18–28)Mn–(9–12)Al–(0.7–1.2)C, strengthened by nano sized κ-carbides. TRIPLEX steels have low densities (6.5–7 g/cm³), high strengths (700–1100 MPa), and high total elongations (≥60%) [8]. Yao et al. [14] studied the strengthening and strain-hardening behavior of aged Fe–30.4Mn–8Al–1.2C lightweight steel and reported that the precipitation of κ-carbides increases the yield strength to 480 MPa without much loss of tensile elongation. Liu et al. [15] investigated the precipitation behavior of inter/intragranular κ-carbides and their effects on

the tensile properties of a hot-rolled Fe–11Mn–10Al–1.25C lightweight steel under different cooling patterns. A nearly full austenitic microstructure with nanosized intragranular κ-carbides was obtained by quenching the material in liquid nitrogen, leading to a strength of 1 GPa at nearly 30% ductility [15]. Adjustment of alloying compositions is an approach to control the precipitation behavior of κ-carbide [16–20]. For example, Mo and Cr suppresses the precipitation behavior of κ-carbide, while Si aids it.

Irrespective of the outstanding tensile properties of Fe–Mn–Al–C-based lightweight steels at room temperature, earlier studies focusing on the effects of an ageing treatment revealed the limits of these materials when exposed to high-temperature environments [20–22]. When lightweight steels with high levels of Al (>9 wt%) and Mn (>30 wt%) are used at temperatures above 550 °C, massive κ-carbide precipitation occurs, accompanied by β-Mn formation, making the matrix brittle, thus dramatically reducing the material's ductility. This is a crucial problem limiting the application of Fe–Mn–Al–C-based lightweight steels. However, it is difficult to find the investigation for improving the high temperature mechanical properties of these materials.

Herein, we report the design and properties of a novel lightweight steel with an excellent combination of strength (491 MPa ultimate tensile strength) and tensile ductility (31 tensile %) at elevated temperature (600 °C). To yield good ductility under these conditions, we had to overturn the conventional Fe–Mn–Al–C-based austenitic design strategy, with the aim to thermally stabilize the microstructure through adequate composition adjustment. We reduced the Al and C contents relative to conventional Fe–Mn–Al–C lightweight steels and added Ti instead. Ti his has three main advantages. First, Ti is in itself a light alloying element. Second, it forms thermally stable Fe_2Ti Laves phase precipitates. Third, it forms nanosized TiC carbides. With these new nanostructure features, we were able to design a novel lightweight steel based on the system Fe–20Mn–6Ti–3Al–0.06C-0.06Nb–3Ni (wt.%) which is both, microstructurally stable and ductile at high temperatures. We refer to this new material as Ti bearing lightweight steel (Ti-LWS, Table 1). Ti-LWS has excellent strength (>490 MPa) and tensile elongation (31%) at elevated temperature (600 °C), as well as 8% lower mass density when compared to pure iron.

2. Experimental procedures

The chemical compositions of the lightweight steels that were examined in this investigation are listed in Table 1. We designed a new lightweight steel based on the Fe–20Mn–6Ti–3Al–0.06C–NbNi (wt%) system by adding Ti to a lightweight steel having lower concentration of Al when compared to conventional Fe–Mn–Al–C-based lightweight steels. The developed steel (Ti-LWS) contained a high amount of Ti. The chemical compositions of the other steel samples (LWS1–LWS5 steel) were within the typical range of conventional austenitic lightweight

steels. As shown in Table 1, the developed steel has higher density than the conventional austenitic lightweight steels, yet it is still much lighter than general steels, with a density reduction of approximately 8%. Ingots were prepared with a commercial vacuum-induction melting furnace. After a 2 h homogenization process in the temperature range of 1100–1150 °C, the ingots were hot-rolled into 12 mm-thick plate samples. The LWS alloys were solution-treated at 1050 °C for 2 h after hot rolling, and then the LWS3, LWS4, and LWS5 samples were finally aged at 550 °C for the designed holding periods for up to 1000 min, as shown in Table 1.

The microstructures of the hot-rolled and aged samples were observed using optical microscopy (OM), scanning electron microscopy (SEM) equipped with an electron backscattered diffraction (EBSD) system (HKL Nordlys Channel 5), and transmission electron microscopy (TEM). The TEM analyses were carried out using thin foil specimens prepared by twin-jet electrolytic polishing. The twin-jet electrolytic polishing was conducted at 25 V and 180 mA with a mixed solution of 10% perchloric acid and 90% methanol at −30 °C. Specimens for EBSD analyses were prepared by mechanical polishing using a colloidal silica suspension for the final polishing stage. An equilibrium phase diagram of the developed steel was calculated using the Thermo-Calc software (TCFE 9 database) and was used to understand the microstructural evolution via the phase transformation.

The mechanical properties of the samples were evaluated by tensile tests and nanoindentation experiments. Tensile tests were performed at room temperature and at an elevated temperature (600 °C) according to the ASTM E8 standard. The plate-type specimens for the tensile tests at room temperature were machined with a gauge length of 25 mm and a width of 6 mm in the reduced parallel section. The round specimens for the tensile tests at 600 °C were machined with a gauge length of 24 mm and a diameter of 6 mm in the reduced parallel section. For the tensile tests at 600 °C, the specimens were initially heated to 600 °C at a rate of 5 °C/min and then held for 20 min at 600 °C prior to testing. Tensile tests were carried out with strain rates of 6×10^{-2} min^{-1} (at room temperature) and 5.2×10^{-3} min^{-1} (at 600 °C) using a universal tensile testing machine. In addition, to assess the intrinsic strengths of the austenite matrix and the Fe_2Ti laves phase in Ti-LWS, nanoindentation tests were carried out at a peak load of 10 mN using a nanoindenter equipped with a Berkovich indenter.

Finally, to understand the influence of the mechanical response of the individual constituent phases on the fracture modes of the developed Ti-LWS at room temperature and at 600 °C, finite element (FE) simulations were conducted using the experimentally observed mechanical data from the nanoindentation and uniaxial tensile tests.

Table 1
Chemical compositions, measured density, and processing conditions for the fabrication of the base alloys.

| Alloy | Chemical bulk comoisition, wt% | | | | | | | | | Density, g/cm³ | Process conditions | |
	Mn	Ti	Al	C	Ni	Nb	Mo	Cr	Fe		Homogenization for hot-rolling	Solution treatment / Ageing treatment
Ti-LWS	19.77	5.97	2.83	0.067	3.01	0.06	–	–	Bal.	7.25	2 h at 1100 °C	No treatment / No treatment
LWS1	24.42	–	8.21	0.98	–	–	–	–	Bal.	6.87	2 h at 1150 °C	2 h at 1050 °C / No treatment
LWS2	24.65	–	8.32	0.97	4.89	–	–	–	Bal.	6.88	2 h at 1150 °C	2 h at 1050 °C / No treatment
LWS3	24.50	–	8.28	0.98	–	–	1.99	–	Bal.	6.87	2 h at 1150 °C	2 h at 1050 °C / 1000 min at 550 °C
LWS4	19.97	–	7.94	0.81	–	–	–	–	Bal.	6.96	2 h at 1150 °C	2 h at 1050 °C / 300 min at 550 °C
LWS5	19.85	–	7.9	0.85	–	–	–	1.49	Bal.	6.88	2 h at 1150 °C	2 h at 1050 °C / 300 min at 550 °C

3. Results

3.1. Multi-phase microstructure and phase transformation behavior of Ti-bearing lightweight steel

Fig. 1 shows the microstructure of the new Ti-LWS alloy after hot rolling (60% reduction at above 900 °C). While conventional Fe–Mn–Al–C-based lightweight steels (LWS1–LWS5 in Table 1) are fully austenitic (γ) with Fe_3AlC-type κ-carbides [23], the Ti-LWS alloy has a very complex microstructure. The SEM image in Fig. 1(a) shows three constituents: (A) a coarse phase with islands, (B) a phase with a lamellar structure, and (C) the surrounding region. The EBSD images in Fig. 1(b) and (c) reveal that the island-type coarse phase (A) and lamellar phase (B) are Fe_2Ti Laves phase with hexagonal structure and γ/Fe_2Ti Laves eutectoid phase, respectively, while the surrounding phase (C) is composed of ferrite (α) with body-centered cubic (BCC) structure. The microstructure of the Ti-LWS alloy was characterized by TEM. Fig. 1(d) shows a bright-field TEM image taken at low magnification. Fig. 1(e) and (f) show the shape and crystallographic information of the Fe_2Ti Laves phases, which are in good agreement with the EBSD results. Interestingly, Fig. 1(g) shows that the DO_3 phase precipitated in the ferrite phase, i.e., phase C in Fig. 1(a) and (b) is partially ordered ferrite.

In addition, fine MX particles with a cuboidal shape were found to be distributed in the austenite matrix as shown in Fig. 1(h). Energy-dispersive X-ray spectroscopy (EDS) revealed that these particles are Ti-enriched MX carbides.

For better understanding of the formation and partitioning of these phases, we conducted thermodynamic calculations using the Thermo-Calc. software (TCFE 9 database), based on the underlying Gibbs free energy equilibria as shown in Fig. 2(a). This suggests the following phase transformation sequence during hot-rolling and cooling. In stage I, during the homogenization (1100 °C) prior to hot rolling, the ferrite, Fe_2Ti Laves, and Ti-enriched MX carbide phases are all stable as shown in Fig. 2(b). The Laves phase forming in this stage is very coarse (4.7 μm in diameter) due to the high diffusion rate of Ti at 1100 °C. Stage II is characterized by the eutectoid reaction of $\alpha \rightarrow \gamma + Fe_2Ti$ Laves phase, occurring during the hot-rolling and initial cooling process as shown in Fig. 2(c). The phase diagram shows that a phase transformation from α to γ occurs, and then the volume fraction of the Laves phase increases from 4.0 to 14.5% in the hot-rolling temperature range of 900–1100 °C and during the initial cooling. The thermodynamic simulations show that the lamellar structure of γ and Fe_2Ti Laves phase forming in stage II occur via the eutectoid reaction of $\alpha \rightarrow \gamma + Fe_2Ti$ Laves phase. During this eutectoid reaction, the Al atoms, a ferrite stabilizer, are rejected
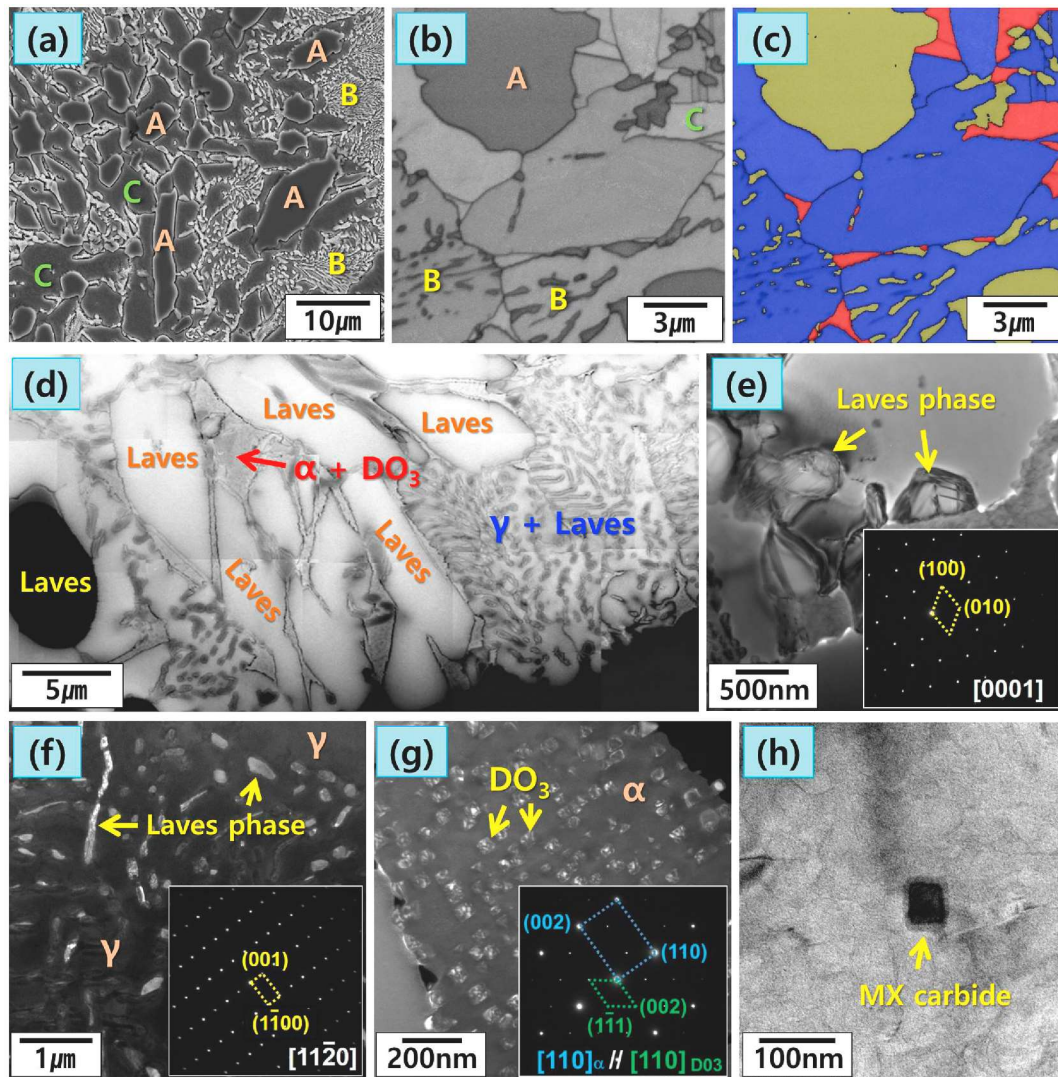

Fig. 1. Microstructure of Ti bearing lightweight steel (Ti-LWS) after hot rolling: (**a**) SEM micrograph, (**b**) EBSD image quality map, and (**c**) EBSD phase map (BCC, FCC, Fe_2Ti Laves). A, coarse phase with islands; B, lamellar phase; C, remaining area. (**d**) TEM image showing the multi-phase microstructure. TEM images and selected area diffraction (SAD) patterns of (**e, f**) Laves phase and (**g**) ordered DO_3 phase. (**h**) TEM image showing the Ti-enriched MX carbide.
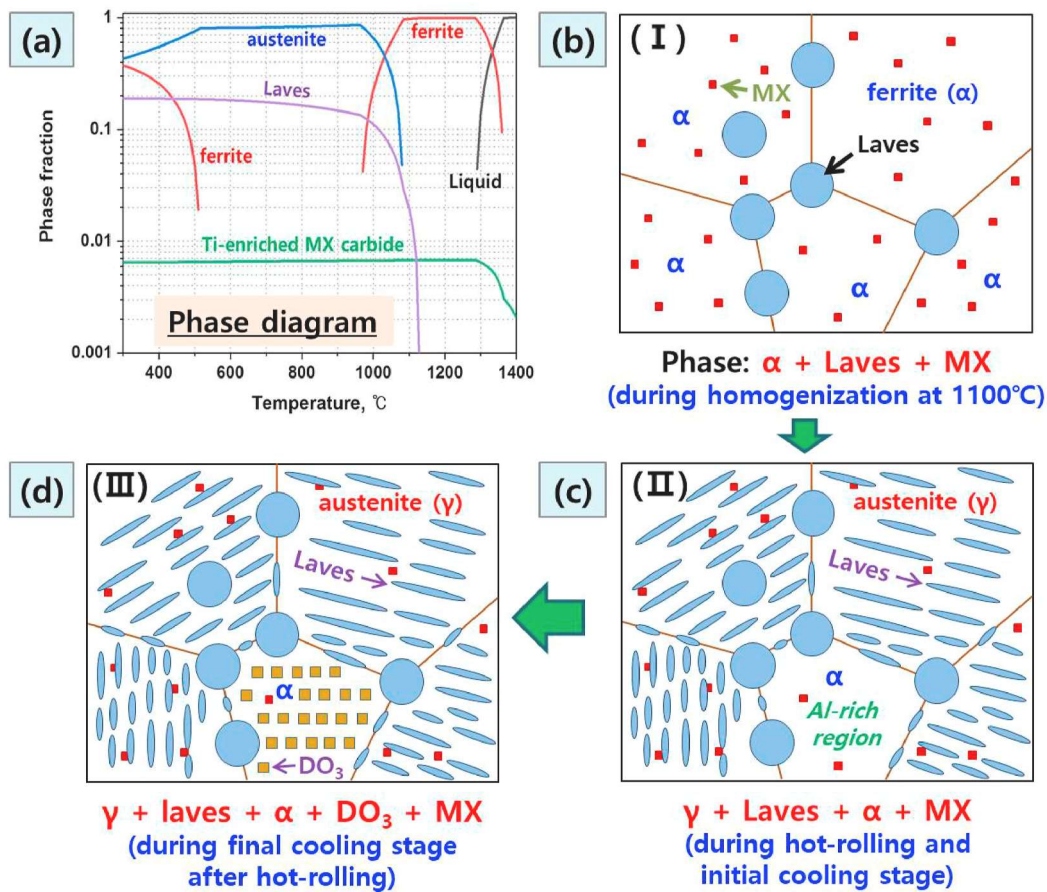
Fig. 2. (a) Equilibrium phase diagram of Ti bearing lightweight steel (Ti-LWS). Schematic illustrations showing the phase transformation sequence during the hot-rolling and cooling processes. (b) Stage I: during homogenization at 1100 °C. (c) Stage II: eutectoid reaction of α → γ + Fe$_2$Ti Laves phase during the hot-rolling and the initial cooling process. (d) Stage III: precipitation of ordered Fe$_3$Al-type DO$_3$ phase in the remaining ferrite regions.

from the transformed γ phase and thereby tend to enrich around the ferrite. EDS analysis (see Fig. 3) supports this sequence. The ferrite region is indeed enriched with Al and depleted of Mn, an austenite stabilizer (see Fig. 3(c)). Finally, in stage III (Fig. 2(d)), the DO$_3$ phase of the Fe$_3$Al type precipitates partially in the Al-enriched ferrite regions as

shown in Figs. 1(g) and Fig. 2(d).

3.2. High temperature tensile properties

Fig. 4 shows the tensile test results both at room temperature and at
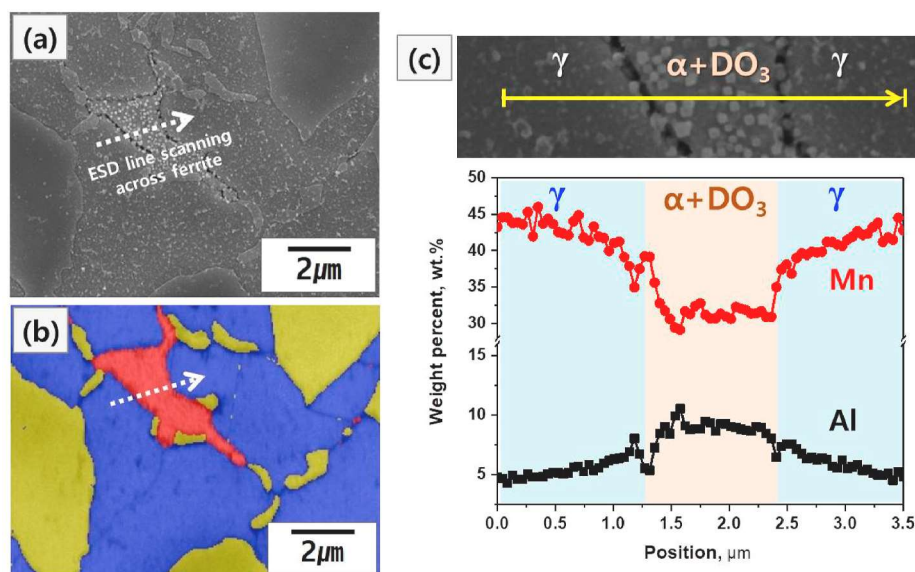
Fig. 3. EDS analyses across the ferrite region: **(a)** SEM micrograph, **(b)** EBSD phase map (BCC, FCC, Fe$_2$Ti laves), and **(c)** EDS line scan profiles for Al and Mn.
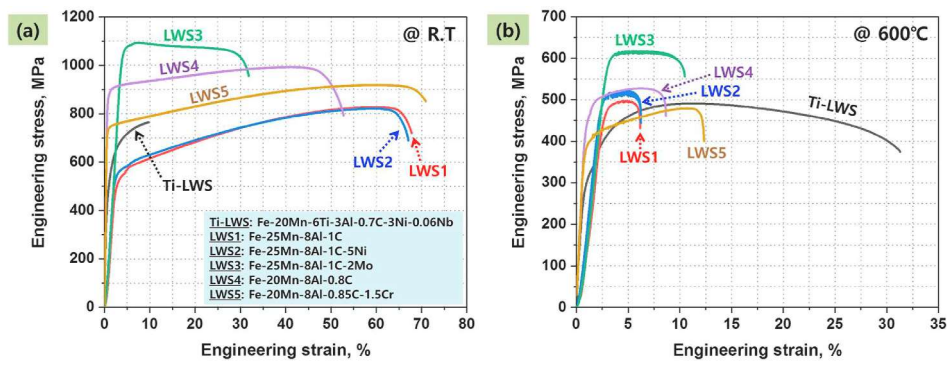
Fig. 4. Engineering stress-strain curves tested at **(a)** room temperature and **(b)** 600 °C.

an elevated temperature (600 °C). Fig. 4(a) shows that the room temperature tensile ductility of the new material is 22.2–61.2% smaller than that of conventional austenitic Fe–Mn–Al–C steels (LWS1-LWS5). This brittle mechanical response is attributed to the presence of the coarse Fe_2Ti Laves phase as shown in Fig. 1. However, at 600 °C, the tensile ductility of conventional lightweight steels was reduced by 21.5–62.4%, whereas that of Ti-LWS was improved by 21.5% as shown in Fig. 4(b). This inverse trend between the new Ti-blended lightweight steel and the conventional lightweight steels is due to the difference in the thermal stability of their underlying microstructures at 600 °C.

Fig. 5(a) and (b) show TEM results of a LWS1 base steel sample after solution treatment at 1050 °C, revealing its simple austenite microstructure. The TEM images in Fig. 5(c) and (e) were taken from the same specimen after tensile testing at 600 °C. Compared to the base steel, tested at room temperature, a strong ordering (Fig. 5(c)) within the austenite matrix and intergranular precipitation of κ-carbides (Fig. 5(e)) are observed. The selected area diffraction (SAD) patterns shown in Fig. 5(d) and (f) indicate that ordered κ-carbides formed in the matrix and along the austenite grain boundaries at 600 °C. This excessive precipitation of κ-carbides led to the deterioration of the material's tensile ductility at 600 °C, as shown in Fig. 4(b). While these κ-carbides strengthen the matrix and grain boundaries at 600 °C, they weaken the solid solution depleted regions adjacent to the grain boundaries. Also, the precipitates at the grain boundaries tend to be incoherent. These effects lead to the observed high temperature embrittlement and the intergranular fracture of conventional lightweight steels (Fig. 5(g)).

The tensile behavior at 600 °C is markedly different for the new Ti-

LWS alloy. Fig. 6(a) and (b) show cross-sectional microstructures near the fracture surface of the material after tensile testing at room temperature and at 600 °C, respectively. Cracks originated at the Fe_2Ti Laves phase precipitates during tensile testing at room temperature, eventually leading to brittle fracture. In contrast, cracks appeared intermittently at the interface between the Fe_2Ti Laves phase and the austenite matrix during tensile testing at 600 °C. Hence, failure occurred by ductile fracture, involving the formation and the coalescence of voids.

4. Discussion

Fig. 6(c) and (d) show representative load–displacement curves of the Fe_2Ti Laves phase and the austenite matrix obtained from the nanoindentation experiments at room temperature and 600 °C, respectively. The nanoindentation hardness values were converted from the load–displacement curves using the Oliver–Pharr method [20,24] as shown in Fig. 6(e). At room temperature, the Fe_2Ti Laves phase has much higher intrinsic strength than the austenite matrix, whereas the intrinsic strength of both the Fe_2Ti Laves phase and the austenite matrix decreased by 82.8 and 74.1%, respectively, as the temperature increased to 600 °C. The intrinsic strength of the Fe_2Ti Laves phase shown in Fig. 6 (e) matches previously published results; Keitz et al. [25] reported that binary Laves phases with composition AB_2 (A = Zr, Nb, Ta and B = Cr, Fe, Co) have a hardness of approximately 9.0–12.9 GPa at room temperature, while their yield strength decreases on average by 81.8% when the temperature is increased from 1000 to 1200 °C. The results shown in
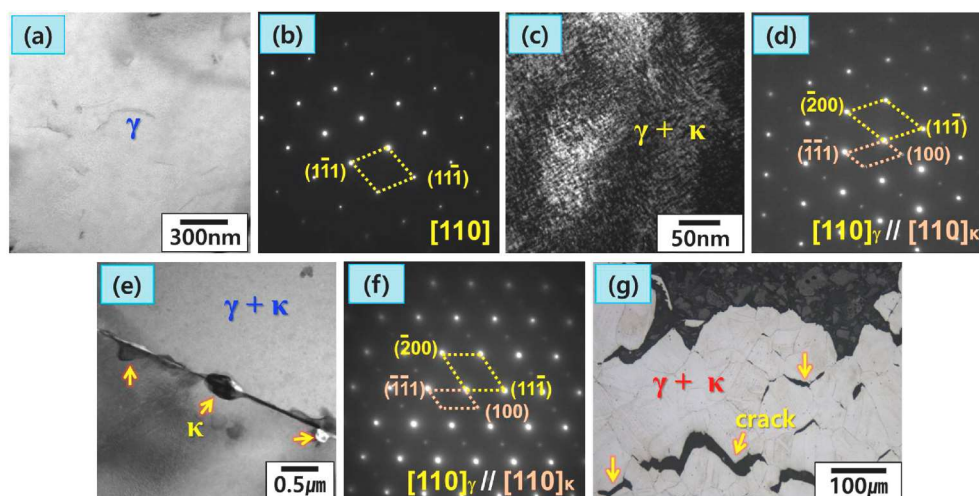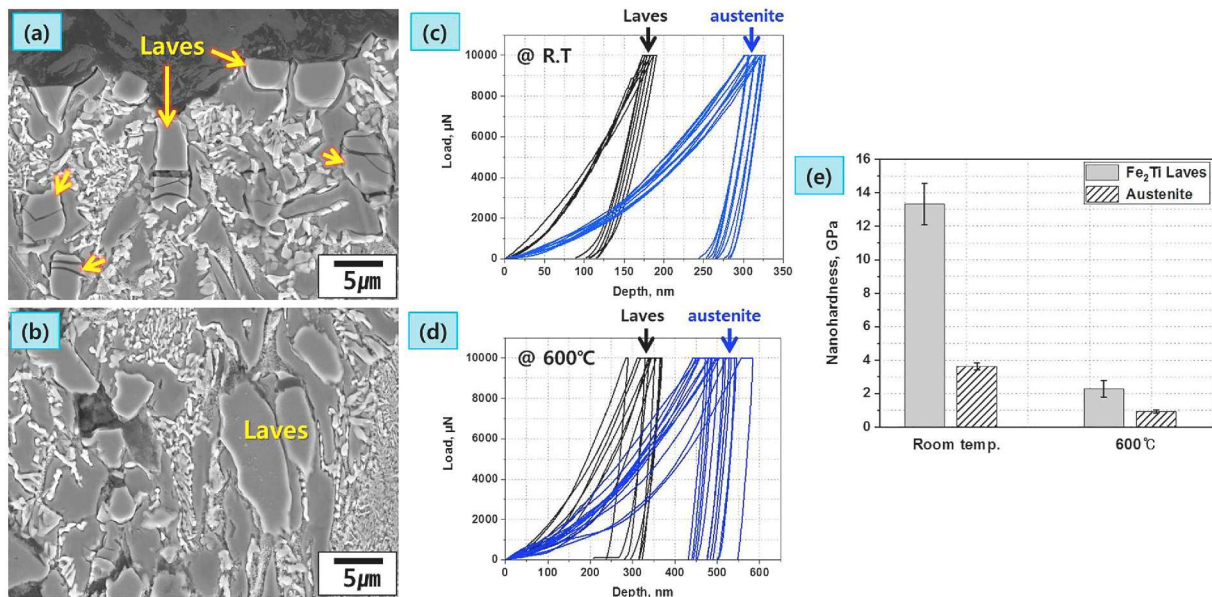

Fig. 5. Microstructure of conventional lightweight steel (LWS1): **(a)** TEM bright-field image and **(b)** SAD pattern of the hot-rolled sample. **(c, e)** TEM bright-field images and **(d, f)** SAD patterns of the sample after tensile testing at 600 °C. **(g)** OM micrograph of the fractured surface showing intergranular cracks after tensile testing at 600 °C.

Fig. 6. SEM micrographs showing the fracture surface of Ti bearing lightweight steel (Ti-LWS) after tensile tests at (**a**) room temperature and (**b**) 600 °C. Nano-indentation load–displacement curves measured at (**c**) room temperature and (**d**) 600 °C for Fe$_2$Ti Laves phase and austenite. (**e**) Nanohardness obtained from the nanoindentation experiments.

Fig. 6 reveal some of the underlying fracture mechanisms in the new Ti-doped alloy at room and elevated temperature. At room temperature, the stress is concentrated inside the brittle secondary phase (Fe$_2$Ti Laves phase) during tensile testing, leading to brittle fracture as shown in Fig. 4(a). At the elevated temperature, the Fe$_2$Ti Laves phase becomes soft, thus better co-deforming with the austenite matrix under tensile load, resulting in the overall high elongation shown in Fig. 4(b).

To reveal the effect of the individual constituent phase on the fracture behavior of the developed Ti-LWS at room temperature and at 600 °C, FE simulations were carried out. In the simulations, the Fe$_2$Ti Laves phase and the austenitic matrix were assumed to behave isotropic elasto-plastic. To obtain macroscopic mechanical properties such as the flow stress curve of each phase, which cannot be readily obtained from nanoindentation, inverse FE calibrations were performed to achieve best fits of the measured nanoindentation load–displacement curves. Fig. 7 (a) and (c) show the fitted nanoindentation load–displacement curves at room temperature and 600 °C, respectively. This approach allowed the identification of the flow stress curves of the Fe$_2$Ti Laves phase and austenite, shown in Fig. 7(b) and (d). We find that the calculated overall flow stress curves for the Ti-LWS bulk material with a given volume fraction of Laves (19 vol%) and austenite phases (80 vol%) agree well with the experimental results for both temperatures. For the FE simulation, the flow stress curves were expressed as a power-law type Swift hardening law, $\sigma = K (\varepsilon_0 + \varepsilon)^n$, when σ and ε represent the stress and the plastic strain, respectively, and the other symbols represent material constants. For the yield function, the isotropic von Mises criterion was adopted. The identified mechanical properties in terms of isotropic elastic-plasticity are summarized as follows. Young's moduli of austenite at room temperature and 600 °C are 200 and 120 GPa, respectively, while those of Laves are 242 and 149 GPa, respectively [26,27]. The Poisson's ratio was assumed to be 0.3 for all cases. Also, the plastic hardening parameters of austenite at room temperature and 600 °C are $(K, \varepsilon_0, n) = (1067$ MPa, 0.0002, 0.18) and (709.3 MPa, 0.002, 0.19), respectively, while those of Laves are $(K, \varepsilon_0, n) = (2548$ MPa, 0.0002, 0.13) and (1377 MPa, 0.0004, 0.12), respectively. The identified mechanical properties were then employed for fracture simulations under tension for the two temperatures, the results of which are shown in Fig. 7 (e) and (f). A simple representative microstructure was constructed from three-dimensional continuum FE elements using an extruded, viz.

columnar grain model. An implicit FE software ABAQUS/Standard was used for the simulation with a reduced integration. For the individual fracture responses of the Laves phases and the austenitic matrix, the principal stress and equivalent plastic strain-based failure criteria were employed, according to the brittleness of the two phases. The boundary conditions impose tension up to the measured fracture strains of the Ti-LWS at the two temperatures. The resultant fracture stress of the Fe$_2$Ti Laves phase at room temperature was 1194 MPa, and the true (logarithmic) fracture strain of austenite at 600 °C was 1.05. With these estimated values, the simulations yielded major failure modes similar to the results obtained from the tensile tests shown in Fig. 6(a) and (c). This means that the brittle failure of the Fe$_2$Ti Laves phase occurred at room temperature when locally exceeding the critical failure stress. The ductile failure of the austenite matrix occurred at the elevated temperature, especially at the interface between the Fe$_2$Ti Laves phases and the matrix, where the local strain exceeded the fracture strain of the austenite, owing to the high mechanical contrast at these hetero-interfaces. There is a transition between the two failure modes, depending on the relative differences in the strength and flow response of the Fe$_2$Ti Laves phase and the austenite matrix as a function of temperature.

5. Conclusion

In summary, we developed a new multiphase lightweight steel based on the system Fe–20Mn–6Ti–3Al–0.06C–Nb–Ni (wt%) which exhibits an excellent combination of strength (491 MPa ultimate tensile strength) and tensile ductility (31%) at high temperatures (600 °C), an application regime hitherto less accessible to weight-reduced steels. The material has a complex microstructure consisting of austenite, partially ordered ferrite, Fe$_2$Ti Laves phase, and fine Ti-enriched MX carbides. While the ductility of conventional lightweight steels decreases significantly at elevated temperatures due to the precipitation of inter/intragranular κ-carbides, the ductility of the new alloy with 31% is 2.5 times more formable at elevated temperatures. This is attributed to the high thermal stability of the microstructure and the improved ductility of the Fe$_2$Ti Laves phases at high temperature. The new material opens up a new application field for the damage-tolerant and lightweight design of structural parts exposed to high temperatures.
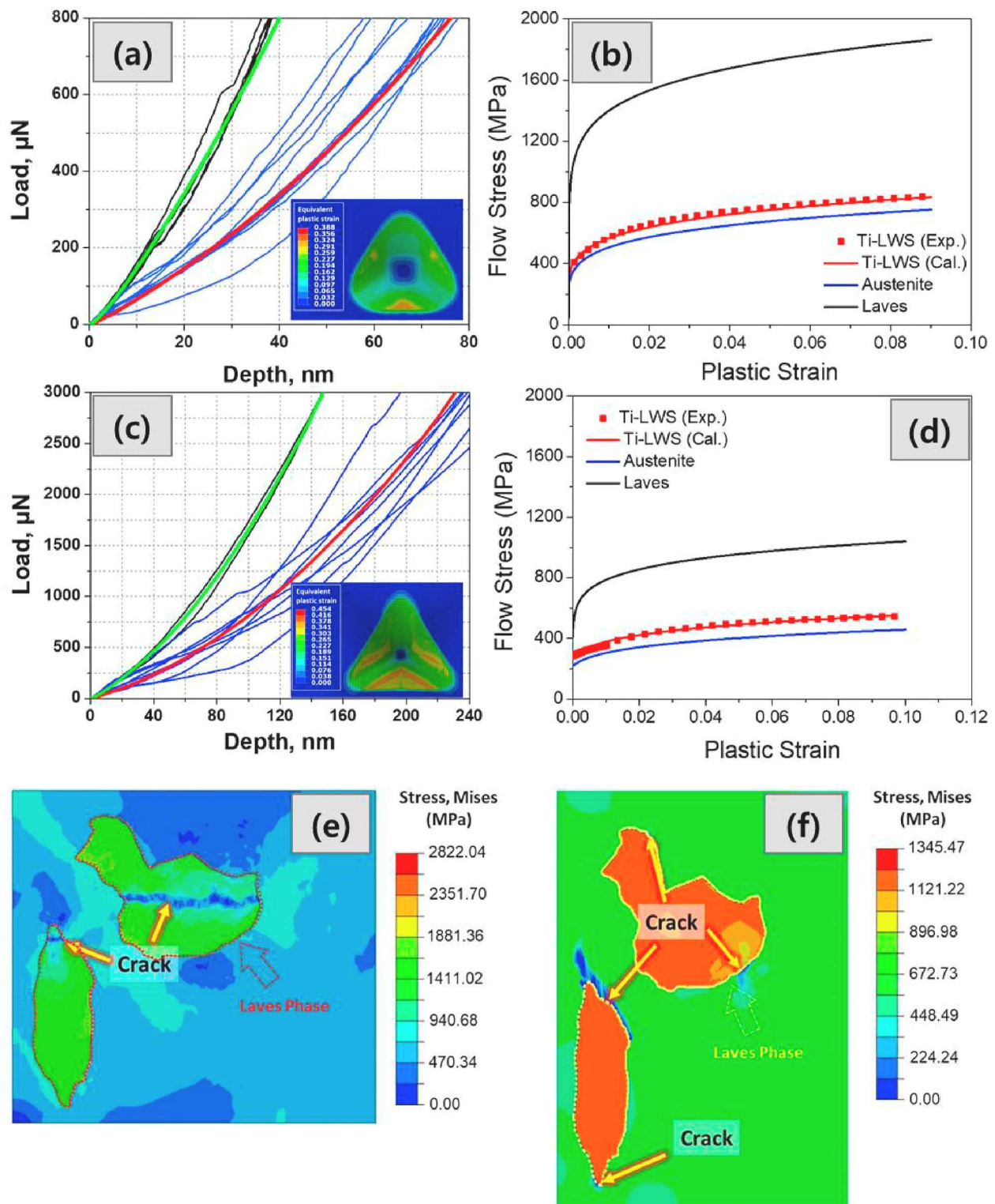
Fig. 7. Measured and simulated nanoindentation load–displacement curves at (**a**) room temperature and (**c**) 600 °C. The flow curves of the Laves phase and the austenite have been iteratively calibrated with the help of the FE simulations to match the measured curves, which resulted in flows stress values for the Laves and austenite at (**b**) room temperature and (**d**) 600 °C. Simulated fractured microstructure of Ti bearing lightweight steel (Ti-LWS) after tensile tests at (**e**) room temperature and (**f**) 600 °C. The color code in (e) and (f) represents the equivalent stress. (For interpretation of the references to color in this figure legend, the reader is referred to the Web version of this article.)

Data availability

The raw/processed data required to reproduce these findings cannot be shared at this time as the data also forms part of an ongoing study.

CRediT authorship contribution statement

Joonoh Moon: Supervision, Investigation, Writing - original draft, supervised this investigation and wrote the manuscript. **Hyo-Haeng Jo:**

prepared the samples and carried out the major experimental works. **Seong-Jun Park:** discussed the results and advised on the manuscript. **Sung-Dae Kim:** Formal analysis. **Tae-Ho Lee:** Formal analysis. **Chang-Hoon Lee:** discussed the results and advised on the manuscript. **Myoung-Gyu Lee:** discussed the deformation behavior at room temperature and 600 °C through the FEM simulation. **Hyun-Uk Hong:** discussed the results and advised on the manuscript. **Dong-Woo Suh:** discussed the results and advised on the manuscript. **Dierk Raabe:** revised the manuscript and contributed to the discussion.

Declaration of competing interest

The authors declare that they have no known competing financial interests or personal relationships that could have appeared to influence the work reported in this paper.

Acknowledgements

References

[1] D. Raabe, C.C. Tasan, E.A. Olivetti, Strategies for improving the sustainability of structural metals, Nature 575 (2019) 64–74, https://doi.org/10.1038/s41586-019-1702-5.

[2] H. Kim, D.-W. Suh, N.J. Kim, Fe-Al-Mn-C lightweight structural alloys: a review on the microstructures and mechanical properties, Sci. Technol. Adv. Mater. 14 (2013) 1–11, https://doi.org/10.1088/1468-6996/14/1/014205.

[3] Y. Kwon, J.H. Hwang, H.C. Choi, T.T.T. Trang, B. Kim, A. Zargaran, N.J. Kim, Microstructure and tensile properties of ferritic lightweight steel produced by twin-roll casting, Met. Mater. Int. 26 (2020) 75–82, https://doi.org/10.1007/s12540-019-00314-2.

[4] A. Zargaran, H.S. Kim, J.H. Kwak, N.J. Kim, Effect of C content on the microstructure and tensile properties of lightweight ferritic Fe-8Al-5Mn-0.1Nb alloy, Met. Mater. Int. 21 (2015) 79–84. https://doi: 10.1007/s12540-015-1009-5.

[5] S.S. Sohn, H. Song, B.-C. Suh, J.-H. Kwak, B.-J. Lee, N.J. Kim, S. Lee, Novel ultra-high-strength (ferrite + austenite) duplex lightweight steels achieved by fine dislocation substructures (Taylor lattices), grain refinement, and partial recrystallization, Acta Mater. 96 (2015) 301–310, https://doi.org/10.1016/j.actamat.2015.06.024.

[6] G. Park, C.H. Nam, A. Zargaran, N.J. Kim, Effect of B2 morphology on the mechanical properties of B2-strengthened lightweight steels, Scripta Mater. 165 (2019) 68–72, https://doi.org/10.1016/j.scriptamat.2019.02.013.

[7] J. Moon, S.-J. Park, S.-D. Kim, J.H. Jang, T.-H. Lee, C.-H. Lee, B.H. Lee, H.-U. Hong, H.N. Han, Phase transformation mechanism and hardness during ageing of an austenitic Fe-30Mn-10.5Al-1.1C-3Mo lightweight steel, J. Alloys Compd. 804 (2019) 511–520, https://doi.org/10.1016/j.jallcom.2019.06.362.

[8] G. Frommeyer, U. Brüx, Microstructures and mechanical properties of high-strength Fe-Mn-Al-C light-weight TRIPLEX steels, Steel Res. Int. 77 (2006) 627–633, https://doi.org/10.1002/srin.200606440.

[9] D. Raabe, H. Springer, I. Gutierrez-Urrutia, F. Roters, M. Bausch, J.-B. Seol, M. Koyama, P.-P. Choi, K. Tsuzaki, Alloy design, combinatorial synthesis, and microstructure-property relations for low-density Fe-Mn-Al-C austenitic steels, JOM 66 (2014) 1845–1856, https://doi.org/10.1007/s11837-014-1032-x.

[10] O.A. Zambrano, A general perspective of Fe-Mn-Al-C steels, J. Mater. Sci. 53 (2018) 14003–14062, https://doi.org/10.1007/s10853-018-2551-6.

[11] I. Zuazo, B. Hallstedt, B. Lindahl, M. Selleby, M. Soler, A. Etienne, A. Perlade, D. Hasenpouth, V. Massardier-Jourdan, S. Cazottes, X. Kleber, Low-density steels: complex metallurgy for automotive applications, JOM 66 (2014) 1747–1758, https://doi.org/10.1007/s11837-014-1084-y.

[12] S. Chen, R. Rana, A. Haldar, R.K. Ray, Current state of Fe-Mn-Al-C low density steels, Prog. Mater. Sci. 89 (2017) 345–391, https://doi.org/10.1016/j.pmatsci.2017.05.002.

[13] K.-T. Park, Tensile deformation of low-density Fe-Mn-Al-C austenitic steels at ambient temperature, Scripta Mater. 68 (2013) 375–379, https://doi.org/10.1016/j.scriptamat.2012.09.031.

[14] M.J. Yao, E. Welsch, D. Ponge, S.M.H. Haghighat, S. Sandlöbes, P. Choi, M. Herbig, I. Bleskov, T. Hickel, M. Lipinska-Chwalek, P. Shanthraj, C. Scheu, S. Zaefferer, B. Gault, D. Raabe, Strengthening and strain hardening mechanisms in a precipitation-hardened high-Mn lightweight steel, Acta Mater. 140 (2017) 258–273, https://doi.org/10.1016/j.actamat.2017.08.049.

[15] D. Liu, M. Cai, H. Ding, D. Han, Control of inter/intra-granular κ-carbides and its influence on overall mechanical properties of a Fe-11Mn-10Al-1.25C low density steel, Mater. Sci. & Eng. A 715 (2018) 25–32, https://doi.org/10.1016/j.msea.2017.12.102.

[16] C.W. Kim, S.I. Kwon, B.H. Lee, J.O. Moon, S.J. Park, J.H. Lee, H.U. Hong, Atomistic study of nano-sized κ-carbide formation and its interaction with dislocations in a cast Si added FeMnAlC lightweight steel, Mater. Sci. & Eng. A 673 (2016) 108–113, https://doi.org/10.1016/j.msea.2016.07.029.

[17] L.N. Bartlett, D.C.V. Aken, J. Medvedeva, D. Isheim, N.I. Medvedeva, K. Song, An atom probe study of kappa carbide precipitation and the effect of silicon addition, Metall. Trans. A 45 (2014) 2421–2435, https://doi.org/10.1007/s11661-014-2187-3.

[18] J. Moon, H.-Y. Ha, S.-J. Park, T.-H. Lee, J.H. Jang, C.-H. Lee, H.N. Han, H.-U. Hong, Effect of Mo and Cr additions on the microstructure, mechanical properties and pitting corrosion resistance of austenitic Fe-30Mn-10.5Al-1.1C lightweight steels, J. Alloys Compd. 775 (2019) 1136–1146, https://doi.org/10.1016/j.jallcom.2018.10.253.

[19] J. Moon, S.-J. Park, J.H. Jang, T.-H. Lee, C.-H. Lee, H.-U. Hong, H.N. Han, J. Lee, B.H. Lee, C. Lee, Investigations of the microstructure evolution and tensile deformation behavior of austenitic Fe-Mn-Al-C lightweight steels and the effect of Mo addition, Acta Mater. 147 (2018) 226–235, https://doi.org/10.1016/j.actamat.2018.01.051.

[20] J. Moon, S.-J. Park, J.H. Jang, T.-H. Lee, C.-H. Lee, H.-U. Hong, D.-W. Suh, S.H. Kim, H.N. Han, B.H. Lee, Atomistic investigations of κ-carbide precipitation in austenitic Fe-Mn-Al-C lightweight steels and the effect of Mo addition, Scripta Mater. 127 (2017) 97–101, https://doi.org/10.1016/j.scriptamat.2016.08.036.

[21] K. Lee, S.-J. Park, J. Lee, J. Moon, J.-Y. Kang, D.-I. Kim, J.-Y. Suh, H.N. Han, Effect of aging treatment on microstructure and intrinsic mechanical behavior of Fe-31.4Mn-11.4Al-0.89C lightweight steel, J. Alloys Compd. 656 (2016) 805–811, https://doi.org/10.1016/j.jallcom.2015.10.016.

[22] I. Kalashnikov, O. Acselrad, A. Shalkevich, L.C. Pereira, Chemical composition optimization for austenitic steels of the Fe-Mn-Al-C system, J. Mater. Eng. Perform. 9 (2000) 597–602, https://doi.org/10.1361/105994900770345430.

[23] J. Moon, S.-J. Park, C. Lee, H.N. Han, T.-H. Lee, C.-H. Lee, Microstructure evolution and age-hardening behavior of microalloyed austenitic Fe-30Mn-9Al-0.9C lightweight steels, Metall. Trans. A 48 (2017) 4500–4510, https://doi.org/10.1007/s11661-017-4265-9.

[24] W.C. Oliver, An improved technique for determining hardness and elastic modulus using load and displacement sensing indentation experiments, J. Mater. Res. 7 (1992) 1564–1583, https://doi.org/10.1557/JMR.1992.1564.

[25] A.V. Keitz, G. Sauthoff, G, Laves phases for high temperatures—Part II: stability and mechanical properties, Intermetallics 10 (2002) 497–510, https://doi.org/10.1016/S0966-9795(02)00025-0.

[26] ASM aerospace specification metals inc. http://asm.matweb.com/search/SpecificMaterial.asp?bassnum=mq304a.

[27] A.A. Gorni, Steel Forming and Heat Treating Handbook, 2012.